catalysts

MDPI

Article

Dual-Vacancy Engineering in Amorphous NiCo Oxyhydroxide Enables Selective Glycerol Electrooxidation to Formic Acid

Zepan Sun [1,†], Yanzheng Feng [1,†], Guanjie Li [2], Ming Xu [2,*], Jing Ma [2], Runzhe Ma [1], Wenting Yang [1] and Tingting Cui [2,*]

[1] College of Aulin, Northeast Forestry University, Harbin 150040, China; zepansun@nefu.edu.cn (Z.S.); yanzhengfeng@nefu.edu.cn (Y.F.); ramsey18746767763@nefu.edu.cn (R.M.); enid031707@163.com (W.Y.)
[2] College of Chemistry, Chemical Engineering and Resource Utilization, Center for Innovative Research in Synthetic Chemistry and Resource Utilization, Northeast Forestry University, Harbin 150040, China; gjieli@126.com (G.L.); majing@nefu.edu.cn (J.M.)
* Correspondence: mingxu@nefu.edu.cn (M.X.); ttcui@nefu.edu.cn (T.C.)
† These authors contributed equally to this work.

Abstract

Electrocatalytic glycerol oxidation to formic acid (FA) offers a sustainable route for biomass valorization, yet non-noble metal catalysts generally suffer from sluggish C-C bond cleavage and poor product selectivity. Here we report an amorphous nickel–cobalt oxyhydroxide bearing both metal and oxygen vacancies (D-NiCoO$_x$H$_y$-V$_{Cr,O}$), grown on nickel foam via one-step electrodeposition followed by electrochemical activation with Cr doping. The coexistence of the dual vacancies is experimentally confirmed by X-ray photoelectron spectroscopy (XPS), which reveals elevated Ni^{3+}/Co^{3+} ratios and reduced lattice oxygen, and by electron paramagnetic resonance (EPR), which shows a markedly enhanced signal at g = 2.003. Building on prior Cr-leaching approaches in single-metal nickel oxides, this work extends dual-vacancy engineering to an amorphous bimetallic NiCo oxyhydroxide and correlates the defect structure with glycerol-induced interfacial responses, charge-transfer behavior, and product selectivity. The catalyst delivers 200 mA cm^{-2} at 1.31 V vs. RHE and achieves 100% Faradaic efficiency for formate at 1.32 V vs. RHE. In situ electrochemical impedance spectroscopy further reveals a significantly reduced charge-transfer resistance. These results establish Cr-assisted dual-vacancy engineering in amorphous bimetallic oxyhydroxides as a promising strategy for selective biomass electrooxidation.

Keywords: vacancy; electrocatalytic; formic acid; glycerol electro-oxidation

Check for updates

Academic Editors: Akira Nishimura and Francisco Pompeo

Received: 6 July 2026
Revised: 14 August 2026
Accepted: 20 August 2026
Published: 21 August 2026

Copyright: © 2026 by the authors. Licensee MDPI, Basel, Switzerland. This article is an open access article distributed under the terms and conditions of the Creative Commons Attribution (CC BY) license.

1. Introduction

Glycerol is the major by-product of biodiesel manufacture and an abundant renewable platform molecule for producing value-added chemicals [1–5]. Owing to its three hydroxyl groups, glycerol oxidation can either retain the carbon skeleton to form C_3 products or involve C-C bond cleavage to generate C_2 and C_1 products [1,3–5]. Formate is particularly attractive because complete conversion of one glycerol molecule can preserve all three carbon atoms within the same C_1 product class, while the anodic glycerol oxidation reaction (GOR) can replace the kinetically sluggish oxygen evolution reaction (OER) in paired electrolysis [4,6–9]. However, formate production requires coordinated glycerol adsorption, dehydrogenation, oxygen-species transfer, C-C bond cleavage, and consecutive oxidation of multicarbon intermediates. Incomplete cleavage leads to the accumulation of glyceraldehyde, glycerate, glycolate, and oxalate, whereas excessive surface oxidation

and competitive OER decrease carbon efficiency and Faradaic efficiency [1,3–9]. Therefore, an effective glycerol-to-formate catalyst must regulate both reaction rate and pathway selectivity rather than merely increase the anodic current.

Electrocatalytic GOR offers mild operating conditions, avoids stoichiometric chemical oxidants, and can be coupled with hydrogen evolution or other cathodic reactions [4,6–9]. Nickel- and cobalt-based (oxy)hydroxides are promising non-noble catalysts because reversible Ni^{2+}/Ni^{3+} and Co^{2+}/Co^{3+} redox transitions can mediate alcohol dehydrogenation, while bimetallic coupling regulates metal-oxygen covalency, interfacial charge transfer, and intermediate adsorption [10–19]. Recent catalyst designs based on hydrogen-bond-network regulation, NiOOH active-phase control, heterointerface construction, foreign-cation incorporation, amorphization, and multimetal electronic modulation have substantially improved GOR kinetics and formate production [10–19]. Nevertheless, most introduced elements remain as stable dopants, alloy components, or interfacial promoters. Such strategies do not directly resolve whether a deliberately generated cation vacancy can cooperate with an oxygen vacancy to separate the functions of substrate adsorption, hydroxyl activation, and C-C bond cleavage on amorphous NiCo oxyhydroxides.

Vacancy engineering provides a direct route to alter coordination number, charge distribution, and adsorption strength at transition-metal sites. Xia et al. reported that selective Cr leaching from NiCrO simultaneously creates Cr-site metal vacancies (V_{Cr}) and oxygen vacancies (V_O), enhances the co-adsorption of OH^- and organic molecules, and promotes glycerol-to-formate conversion [20]. Zhong et al. and Guo et al. showed that oxygen-deficient oxide surfaces provide additional adsorption sites and accelerate interfacial charge transfer [21,22], while Ren et al. linked V_O formation to redistribution of OH^- adsorption sites [23]. In related oxyhydroxide electrocatalysis, Niu et al. demonstrated that Cr vacancies redistribute charge on neighboring metal centers and optimize oxygen-intermediate adsorption [24]. Zhai et al. further reported that multiple cation and oxygen vacancies can regulate high-valent metal formation more effectively than an isolated defect [25], whereas Zhao et al. and Rafei et al. associated cation deficiency or sacrificial-metal dissolution with enhanced metal-oxygen covalency, distorted coordination, and accelerated oxyhydroxide reconstruction [26,27]. These studies indicate that a Cr-induced metal vacancy is not an inert empty site: it can impose undercoordination and electronic redistribution on adjacent Ni/Co centers, while the accompanying V_O provides a chemically distinct environment for hydroxyl adsorption and activation. The unresolved issue is whether these two defects can be deliberately coupled in NiCo oxyhydroxide and assigned complementary catalytic functions rather than treated simply as an increase in total defect density.

Previous mechanistic studies also provide a basis for defining selective C-C bond scission. Zhang et al. reported that electronically coupled Ni/Co sites lower the barrier for active-*OH-mediated C-C cleavage and the subsequent dehydrogenation of C_1 intermediates [28]. Li et al. showed that Pd-Cu dual sites facilitate *OH generation, strengthen glycerol adsorption, and decrease the energy barrier of the C-C-cleavage step [29], whereas Han and Liu demonstrated that a direct C-C-cleavage route can suppress multicarbon side pathways during formate electrosynthesis [30]. Zhang et al. further reported that differential adsorption of glycerol hydroxyl groups at Ni-O-Ce interfaces constrains the substrate in a favorable configuration for directional C-C cleavage [31], and Wang et al. assigned complementary adsorption and cleavage functions to different metal sites in multicomponent nanosheets [32]. Conversely, catalysts and operating strategies that stabilize adsorbed C_3 intermediates, promote their desorption, or alter potential-dependent surface coverage can preserve glycerate or switch the dominant product pathway [33–36]. Suppressing inactive high-valent Ni accumulation and competitive OER also broadens the potential window

for formate formation [37–39]. Accordingly, selective C-C bond scission does not mean indiscriminate rupture of every C-C bond. It denotes preferential adsorption of glycerol and its C_3/C_2 intermediates in cleavage-prone configurations, followed by rapid sequential conversion to C_1 formate, while suppressing C_3 retention, C_2 accumulation, uncontrolled overoxidation, and OER.

The postulation of coupled metal and oxygen vacancies is further supported by studies that separate electronic regulation from oxygen-species activation. Shi et al. reported that modulating the electron density of amorphous NiFe alloys changes oxygen-intermediate adsorption and the formation of active Ni^{3+} species during biomass electrooxidation [40]. Ma et al. demonstrated that cooperative Lewis and Brønsted acid sites promote *OH formation and formate selectivity [41], while Wu et al. showed that closely spaced oxygen vacancies act cooperatively to facilitate charge transfer and the conversion of C_2 intermediates into C_1 products [42]. Other studies have established that interfacial hydrogen bonding, oxygen-vacancy coordination, paired electrolysis, orbital-specific electron donation, and controlled *OH coverage can determine whether oxygenated intermediates undergo C-C cleavage or retain the multicarbon skeleton [43–49]. Beyond GOR, Li et al. reported that phosphorus vacancies in ultrathin RuP nanosheets redistribute local charge and shift the d-band center of neighboring Ru sites [50], and Fang et al. summarized how support interactions, promoters, and adsorption energetics govern bond activation and product selectivity in reforming catalysis [51]. These two studies are not direct GOR analogues, but they reinforce the general defect-catalysis principle that vacancy-induced charge redistribution can tune adsorption and bond activation. Related glycerol electrolysis studies based on high-entropy alloys, Mn-doped nickel phosphides, nickel selenides, vacancy-rich NiO_xH_y, and composition-dependent active oxygen species further connect electronic structure, oxygen adsorption, and product distribution [52–60]. In particular, Chen et al. showed that vacancy-rich NiO_xH_y enables an adsorbed-oxygen-mediated C-C-cleavage pathway that is inaccessible to oxygen-vacancy-poor beta-$Ni(OH)_2$ [56]. Collectively, these results justify a division-of-function hypothesis in which metal vacancies regulate the electron density and adsorption strength of neighboring metal sites, whereas oxygen vacancies regulate hydroxyl uptake and reactive oxygen coverage; their coupling should therefore influence both GOR kinetics and cleavage selectivity.

Previous GOR studies have shown that oxygen vacancies can regulate OH^- adsorption, interfacial charge transfer, and C-C cleavage [21–23,42,56]. More directly, Xia et al. demonstrated that selective Cr leaching in NiCrO simultaneously creates Cr-site metal vacancies and oxygen vacancies and enhances the co-adsorption of OH^- and organic molecules [20]. Relative to these reports, the present work extends Cr-assisted dual-vacancy engineering to an amorphous bimetallic NiCo oxyhydroxide. Cr-assisted electrochemical reconstruction generates coexisting Cr-derived metal and oxygen vacancies, while the combination of XPS and EPR with in situ EIS, glycerol-induced OCP responses, ATR-FTIR, and product analysis correlates the defect-modulated Ni/Co electronic structure with stronger glycerol-surface interaction, lower interfacial charge-transfer resistance, and preferential conversion to C_1 formate. D-NiCoOxHy-$V_{Cr,O}$ reaches 200 mA cm^{-2} at 1.31 V vs. RHE and affords 100% formate Faradaic efficiency at 1.32 V vs. RHE, with competitive activity among reported non-noble-metal GOR catalysts. Thus, the principal contribution is the extension of Cr-assisted dual-vacancy engineering from a single-metal oxide to an amorphous bimetallic oxyhydroxide and the experimental support for a structure–performance relationship between the coexisting vacancies and selective glycerol-to-formate conversion.

2. Results and Discussion

2.1. Synthesis and Structural Characterization of Defect-Rich D-NiCoO$_x$H$_y$-V$_{Cr,O}$

NiCoCrO$_x$H$_y$ was first grown on nickel foam (NF) by a one-step electrodeposition method and then activated by cyclic voltammetry to generate metal and oxygen vacancies (V_M and V_O), affording D-NiCoO$_x$H$_y$-V$_{Cr,O}$ (Figure 1a). A control sample without Cr doping, D-NiCoO$_x$H$_y$, was prepared under identical conditions for comparison. X-ray diffraction (XRD) patterns of both D-NiCoO$_x$H$_y$ and D-NiCoO$_x$H$_y$-V$_{Cr,O}$ show no sharp crystalline diffraction peaks across the 20 to 80 degree range (Figure S1), indicating an amorphous structure for both samples. Transmission electron microscopy (TEM) images reveal that D-NiCoO$_x$H$_y$-V$_{Cr,O}$ adopts a nanosheet morphology (Figures 1b–d and S2) that offers a large specific surface area favorable for exposing active sites. High-resolution TEM (HRTEM) images (Figure 1e,f) show no long-range ordered lattice fringes, only a maze-like disordered contrast consistent with the XRD result, and the corresponding fast Fourier transform (FFT) pattern (Figure 1g) contains only two diffuse concentric rings without discrete diffraction spots, confirming the amorphous nature of the catalyst at the crystallographic level. Energy-dispersive X-ray spectroscopy (EDS) elemental mapping (Figure 1h) shows Ni, Co, Cr, and O uniformly distributed across the nanosheets without detectable agglomeration or segregation. Beyond qualitative EDS mapping, quantitative XPS analysis was performed to accurately determine the surface elemental composition of D-NiCoO$_x$H$_y$-V$_{Cr,O}$. After excluding the ubiquitous surface carbon contamination, the normalized atomic percentages of the inorganic elements were determined to be O = 66.0%, Co = 13.8%, Ni = 13.9%, and Cr = 6.3%. This quantitative composition confirms the successful incorporation of chromium into the NiCo oxyhydroxide lattice at a substantial level. The quantitative XPS data thus provide a rigorous compositional basis for understanding the dual-vacancy formation mechanism and the subsequent electronic modulation of Ni/Co active sites.

2.2. Electronic Structure Modulation via Dual-Defect Engineering

XPS was used to probe the electronic structure of D-NiCoO$_x$H$_y$-V$_{Cr,O}$ and D-NiCoO$_x$H$_y$. The Ni 2p$_{3/2}$ Ni^{2+}/Ni^{3+} ratio of D-NiCoO$_x$H$_y$-V$_{Cr,O}$ is 0.44, and the Co 2p$_{3/2}$ Co^{2+}/Co^{3+} ratio is approximately 0.39 (Table S1). In comparison, for the reference catalyst D-NiCoO$_x$H$_y$, these ratios are 0.56 and 0.83, respectively (Figure 2a,b). Compared with D-NiCoO$_x$H$_y$, D-NiCoO$_x$H$_y$-V$_{Cr,O}$ exhibits an increased proportion of high-valence Ni^{3+} and Co^{3+} species, confirming that Cr-assisted electrochemical activation induces electronic structure reconstruction. The formation of coupled metal and oxygen vacancies modifies the local metal-oxygen coordination environment and promotes the stabilization of electron-deficient Ni/Co active sites. This elevated oxidation state likely arises from two cooperative effects: V_M raises the local electron density at the catalyst surface while V_O withdraws electron density from neighboring metal ions, together stabilizing Ni^{3+}/Co^{3+} species. The positive shift in O 1s binding energies after defect formation indicates a modified oxygen coordination environment. This shift is associated with oxygen vacancy generation, hydroxylation variation, and defect-induced electronic redistribution rather than a simple electron-transfer process between oxygen and metal sites (Figure 2c). The Cr 2p spectrum (Figure 2d) shows that Cr is present in a higher oxidation state after CV activation, consistent with the formation of highly oxidized metal species. The decrease in lattice oxygen indicates that Cr leaching disrupts the regular lattice coordination of the NiCo oxyhydroxide, releasing lattice oxygen atoms and generating abundant surface oxygen vacancies. Together, these results confirm the successful construction of a dual-vacancy system combining V_M and V_O.

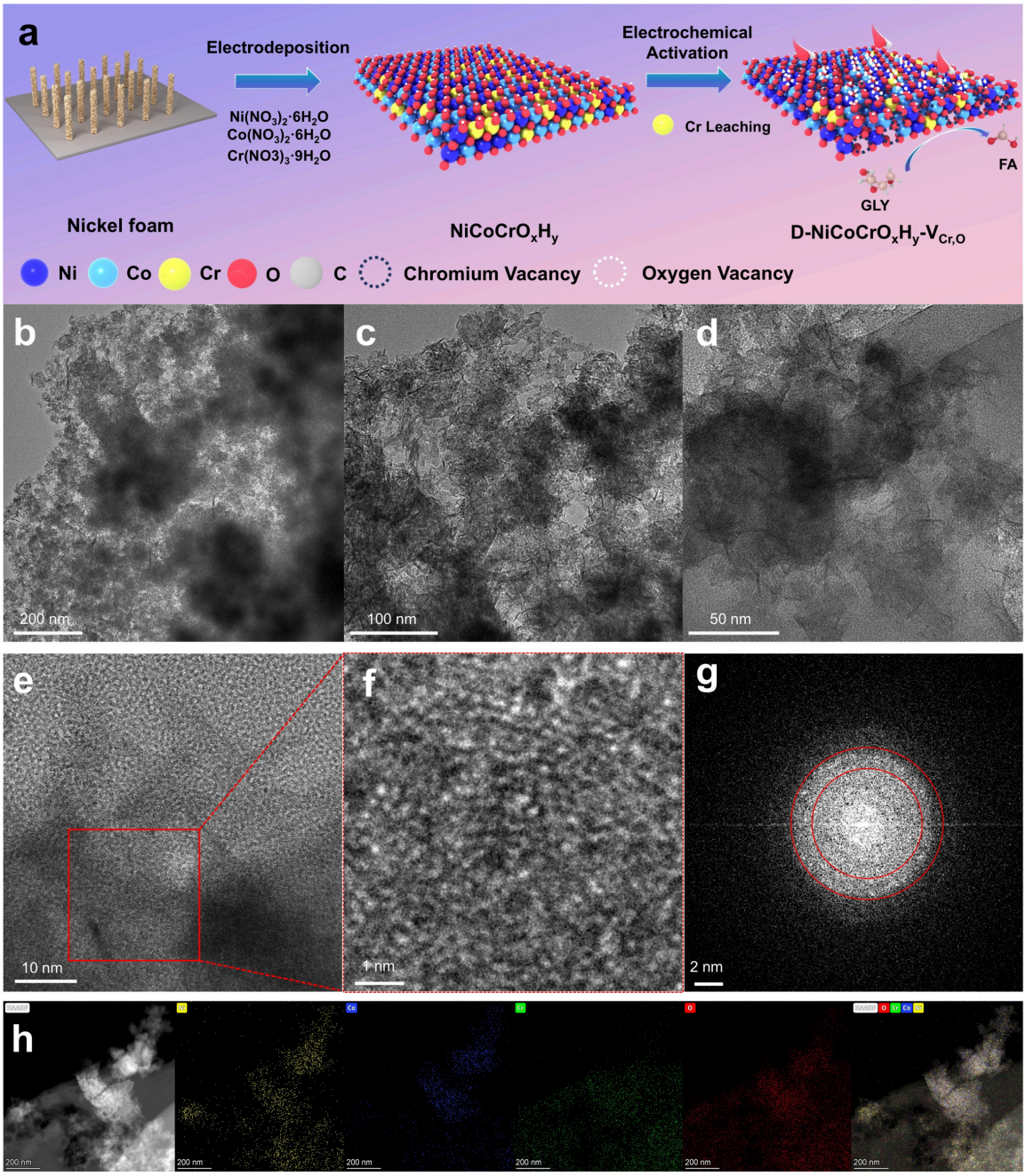


Figure 1. Synthesis and structural characterization of D-$NiCoO_xH_y$-$V_{Cr,O}$. (**a**) Schematic illustration of the synthesis process, including electrodeposition and electrochemical activation in 1.0 M KOH. (**b**–**d**) TEM images of D-$NiCoO_xH_y$-$V_{Cr,O}$. (**e**,**f**) HRTEM images of D-$NiCoO_xH_y$-$V_{Cr,O}$. (**g**) FFT pattern corresponding to (**f**). (**h**) EDS elemental mapping of D-$NiCoO_xH_y$-$V_{Cr,O}$.

The XPS survey spectra further confirm successful Cr incorporation into the NiCo oxyhydroxide lattice, and the Cr signal intensity decreases after CV activation relative to before activation (Figure 2e), indicating partial Cr leaching that generates metal vacancies (V_M) without removing the majority of doped Cr. Moreover, ICP-OES analysis reveals that the Ni:Co:Cr atomic ratio changes from approximately 0.1422:0.2305:0.1077 before activation to 0.1644:0.2393:0.0270 after activation, suggesting substantial Cr leaching and the formation of metal-deficient structures. EPR spectra collected at g = 2.003 show a substantially stronger signal for D-$NiCoO_xH_y$-$V_{Cr,O}$ than for D-$NiCoO_xH_y$ (Figure 2f), confirming a high concentration of V_O in D-$NiCoO_xH_y$-$V_{Cr,O}$. Together, these characterizations establish

the coexistence of V_O and V_M in D-NiCoO$_x$H$_y$-V$_{Cr,O}$ and point to their synergistic role in generating the M-OOH species that drive GOR.

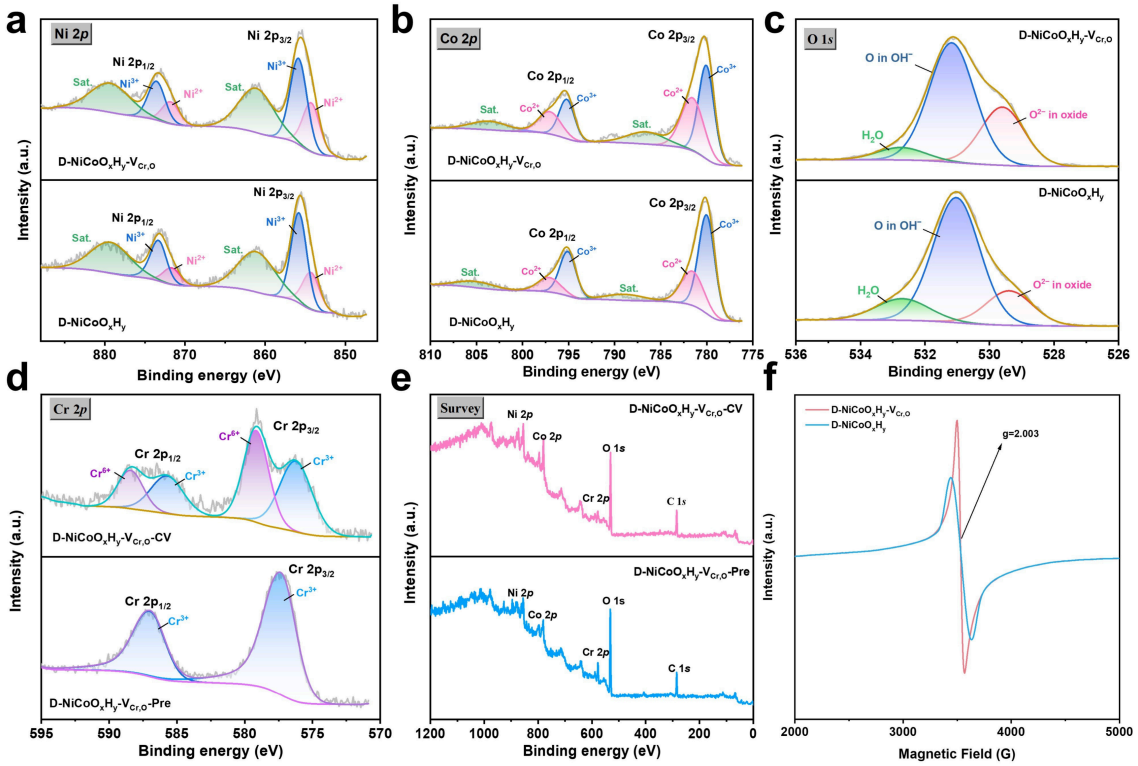


Figure 2. Electronic structure of D-NiCoO$_x$H$_y$-V$_{Cr,O}$ and D-NiCoO$_x$H$_y$. High-resolution XPS spectra of (**a**) Ni 2p, (**b**) Co 2p, (**c**) O 1s, and (**d**) Cr 2p. (**e**) Survey XPS spectra of D-NiCoO$_x$H$_y$-V$_{Cr,O}$ before and after activation. (**f**) EPR spectra of D-NiCoO$_x$H$_y$-V$_{Cr,O}$ and D-NiCoO$_x$H$_y$ at room temperature.

Beyond the steady-state defect characterization, it is essential to clarify how the dual vacancies are kinetically generated during the electrochemical activation process. In the as-deposited NiCoCrO$_x$H$_y$ precursor, the incorporation of Cr^{3+} into the NiCo oxyhydroxide framework introduces local lattice strain and weakens the neighboring M-O (M = Ni, Co) bonding due to the distinct ionic radius and bond energy of Cr^{3+} relative to Ni^{2+}/Co^{3+}. This chemical heterogeneity serves as the structural prerequisite for subsequent vacancy formation. During the subsequent cyclic voltammetry activation in 1.0 M KOH, the applied anodic potential drives the oxidation of Cr^{3+} to soluble high-valent chromate species, which are leached out from the solid lattice. Importantly, this Cr leaching is not a simple ion-exchange process; the rupture of the local M-O-Cr bridges simultaneously removes both the Cr cation and adjacent lattice oxygen atoms that lose their coordination partners, thereby generating coupled V_M and V_O in a single electrochemical corrosion event. In contrast, the Cr-free D-NiCoO$_x$H$_y$ control undergoes the same activation but yields only a marginal EPR signal for VO, confirming that without the sacrificial "structural weak point" provided by Cr, substantial metal vacancies cannot be formed.

2.3. Electrocatalytic GOR Performance

The electrocatalytic GOR performance of D-NiCoO$_x$H$_y$-V$_{Cr,O}$ was evaluated in an H-type cell with 1.0 M KOH electrolyte at ambient temperature. In glycerol-containing electrolyte, D-NiCoO$_x$H$_y$-V$_{Cr,O}$ reaches 100 mA cm^{-2} at 1.28 V vs. RHE, markedly lower than the 1.57 V vs. RHE required for OER at the same current density (Figure 3a), reflecting the kinetically favorable nature of GOR on this catalyst. To optimize the Cr doping level, we prepared samples with different Cr precursor amounts. The LSV curves in Figure S3

show that the standard Cr content gives the best GOR activity; excessive or insufficient Cr both degrade the performance. For Ni-based oxyhydroxide catalysts, the anodic current in this potential region is associated with the Ni^{2+}/Ni^{3+} reconstruction process. However, comparison between glycerol-containing and glycerol-free electrolytes demonstrates that the significantly enhanced current in the presence of glycerol originates from glycerol electrooxidation. In 100 mM glycerol solution, D-$NiCoO_xH_y$-$V_{Cr,O}$ and D-$NiCoO_xH_y$ require 1.31 V and 1.47 V vs. RHE, respectively, to reach 200 mA cm^{-2} (Figure 3b), confirming the superior GOR activity of D-$NiCoO_xH_y$-$V_{Cr,O}$. Tafel analysis (Figure 3d) gives a slope of 84.33 mV dec^{-1} for D-$NiCoO_xH_y$-$V_{Cr,O}$, substantially lower than the 180.32 mV dec^{-1} of D-$NiCoO_xH_y$. Because a smaller Tafel slope reflects faster charge transfer at a given potential, this result confirms that D-$NiCoO_xH_y$-$V_{Cr,O}$ has more favorable GOR kinetics. At potentials of 1.3, 1.35, and 1.4 V vs. RHE, D-$NiCoO_xH_y$-$V_{Cr,O}$ reaches current densities of 147, 320, and 412 mA cm^{-2}, respectively, all substantially higher than those of D-$NiCoO_xH_y$ at the same potentials (Figure 3c). The electrochemical active surface area (ECSA) of the two catalysts was estimated from the electrochemical double-layer capacitance (C_{dl}), derived from CV curves at different scan rates (Figure S4). D-$NiCoO_xH_y$-$V_{Cr,O}$ shows a C_{dl} of 1.69 mF cm^{-2}, higher than the 0.99 mF cm^{-2} of D-$NiCoO_xH_y$ (Figure 3e), indicating that the coupled vacancies expose more active sites. The current densities shown in Figure 3 were normalized by the geometric electrode area. Although D-$NiCoO_xH_y$-$V_{Cr,O}$ exhibits a larger electrochemically active surface area due to the defect-rich nanosheet structure, the higher ECSA-normalized current density further confirms that the enhanced GOR performance originates not only from increased electrochemically accessible surface area but also from the intrinsic electronic modulation of Ni/Co active sites induced by coupled metal and oxygen vacancies (Figure S5). Beyond the geometric current density, we further evaluated the intrinsic catalytic activity using mass activity and ECSA-normalized specific activity to provide a comprehensive benchmark. The mass activity of D-$NiCoO_xH_y$-$V_{Cr,O}$ at 1.28 V vs. RHE reaches 12.99 mA mg^{-1}, based on the total catalyst loading of 7.7 mg on the electrode. Notably, the ECSA-normalized specific activity, derived from the C_{dl} with a specific capacitance of 0.04 mF cm^{-2} for Ni/Co-based hydroxides in alkaline media, is calculated to be 1.99 mA cm^{-2} at the same potential. Benchmarking against previously reported catalysts further shows that D-$NiCoO_xH_y$-$V_{Cr,O}$ requires a lower potential to reach 100 mA cm^{-2} than most non-noble-metal GOR catalysts (Figure 3f). To assess the reproducibility of the electrochemical measurements, all LSV, CV, and EIS measurements were independently repeated at least three times using separately prepared electrode batches (Figures S6 and S7).

2.4. Reaction Kinetic Analysis via In Situ EIS

To gain further insight into how the dual-vacancy structure enhances GOR kinetics, in situ electrochemical impedance spectroscopy (EIS) measurements were performed over a frequency range of 10^{-2} to 10^3 Hz at stepwise increasing potentials, with the results summarized in Figure 4.

The 3D Bode phase plots of D-$NiCoO_xH_y$-$V_{Cr,O}$ and D-$NiCoO_xH_y$ (Figure 4a,c) show two distinguishable processes across the measured frequency range. The high-frequency phase angle peak (10 to 10^3 Hz) reflects charge transport within the electrode bulk together with electrochemical oxidation and reconstruction of the catalyst, while the low-frequency response (10^{-2} to 1 Hz) corresponds to the interfacial Faradaic charge transfer associated with GOR. As the applied potential increases, the low-frequency phase angle peak of both catalysts attenuates, consistent with accelerated interfacial kinetics at higher driving force. This attenuation is markedly faster for D-$NiCoO_xH_y$-$V_{Cr,O}$ than for D-$NiCoO_xH_y$ across both frequency regions, showing that the dual-vacancy structure accelerates both bulk

charge transport and interfacial GOR kinetics, consistent with the lower Tafel slope and superior polarization performance described above.

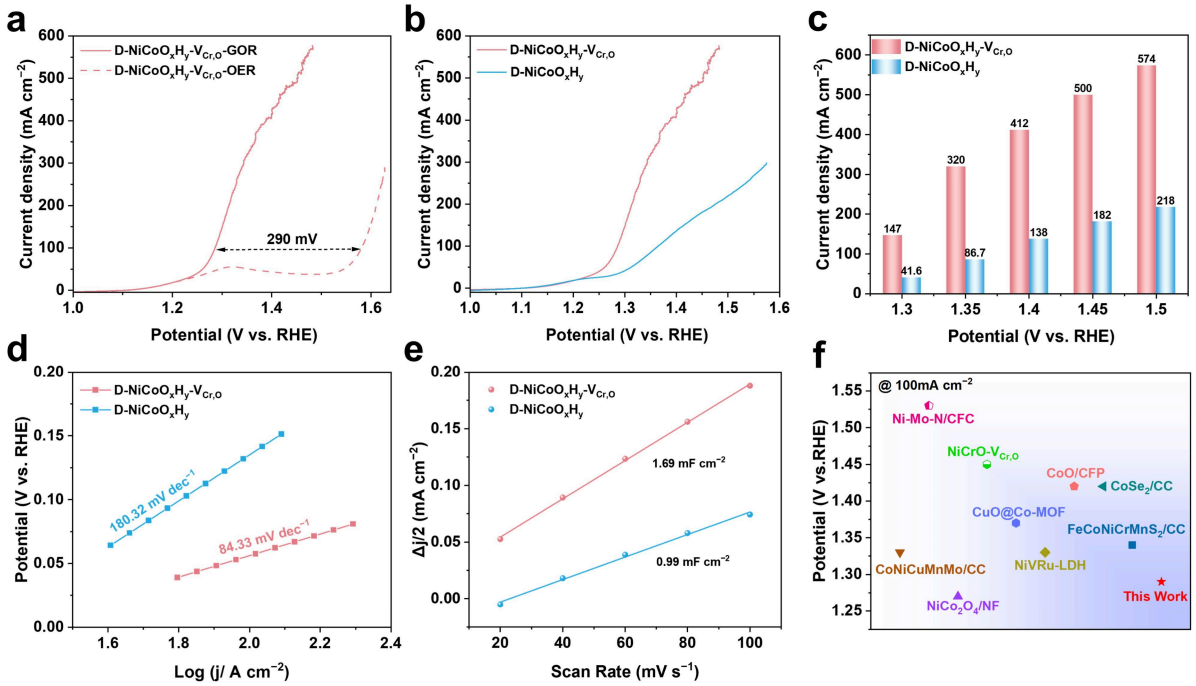


Figure 3. Electrocatalytic GOR performance of D-NiCoO$_x$H$_y$-V$_{Cr,O}$. (**a**) Polarization curves of D-NiCoO$_x$H$_y$-V$_{Cr,O}$ for OER and GOR in 100 mM glycerol solution. (**b**) GOR polarization curves of D-NiCoO$_x$H$_y$-V$_{Cr,O}$ and D-NiCoO$_x$H$_y$ in 100 mM glycerol solution. (**c**) Current densities at potentials from 1.3 to 1.5 V vs. RHE. (**d**) Tafel plots. (**e**) Double-layer capacitance (C$_{dl}$). (**f**) Comparison of the potential required for 100 mA cm^{-2} with recently reported non-noble-metal GOR electrocatalysts.

The corresponding Nyquist plots (Figure 4b,d), in which the semicircle diameter in the high-to-medium frequency region reflects the charge transfer resistance (R$_{ct}$), show progressively smaller semicircles for both catalysts as the potential increases, consistent with a lower reaction barrier and faster interfacial electron transfer at higher potential. The fitted charge-transfer resistances are summarized in Tables S2 and S3 for D-NiCoO$_x$H$_y$-V$_{Cr,O}$ and D-NiCoO$_x$H$_y$, respectively. Across the entire potential range, the defect-rich catalyst exhibits consistently lower R$_{ct}$ values, confirming its superior interfacial charge-transfer kinetics. Above 1.25 V vs. RHE, D-NiCoO$_x$H$_y$-V$_{Cr,O}$ exhibits a substantially smaller semicircle, and thus a much lower R$_{ct}$, than D-NiCoO$_x$H$_y$, providing direct evidence that the dual-vacancy structure optimizes interfacial charge transfer. This improvement reflects the complementary roles of the two vacancies: metal vacancies enhance the intrinsic electrical conductivity of the surface, while oxygen vacancies promote hydroxyl adsorption and the formation of active intermediates, together lowering the resistance to electron exchange between reactants and active sites.

At higher potentials, the decline in R$_{ct}$ for D-NiCoO$_x$H$_y$-V$_{Cr,O}$ slows slightly and the low-frequency phase angle remains somewhat elevated relative to the low-potential range. Rather than a kinetic disadvantage, this reflects strong substrate adsorption at the electron-deficient metal sites of the dual-vacancy surface, where the abundant vacancies enhance adsorption of glycerol and reaction intermediates. Under fast-reaction conditions at high potential, transient accumulation of adsorbed intermediates slightly raises the interfacial mass transfer resistance, consistent with the enhanced adsorption capacity confirmed by the open-circuit potential measurements below. This strong adsorption enriches reactants

at the active sites and promotes subsequent C-C bond cleavage, contributing to the high GOR activity and selectivity of D-NiCoO$_x$H$_y$-V$_{Cr,O}$.

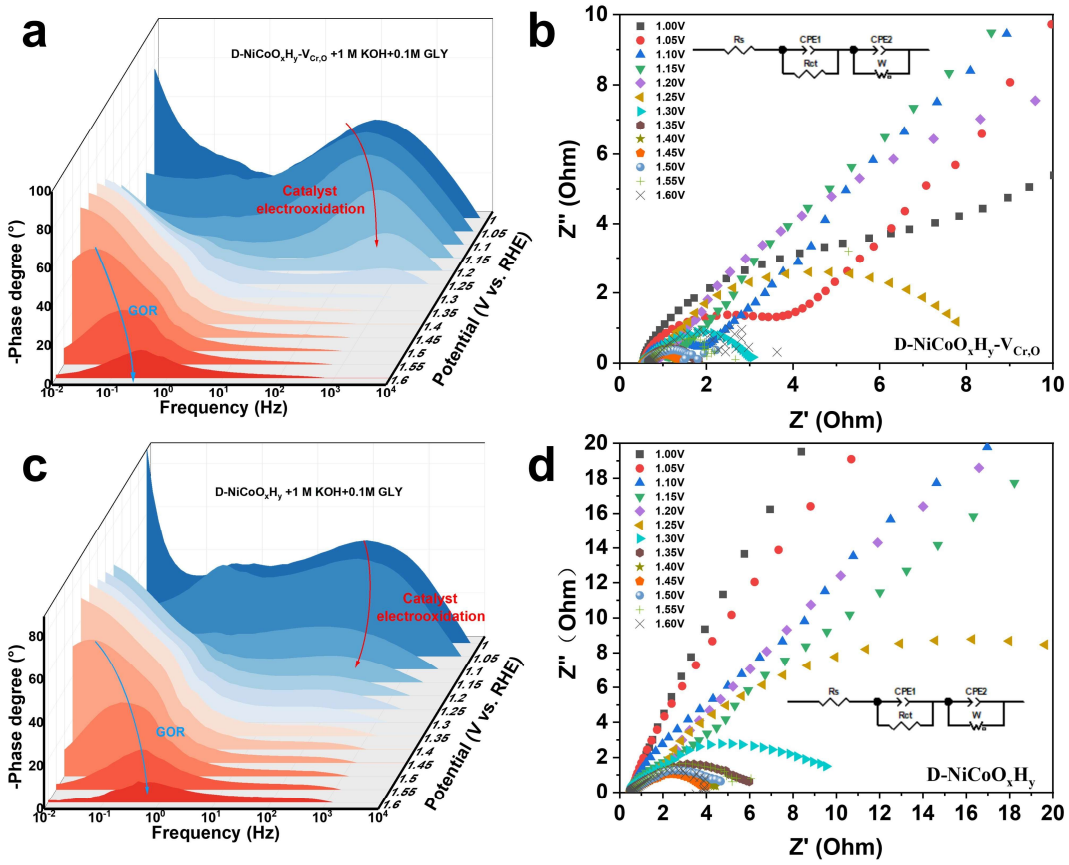


Figure 4. In situ EIS analysis during GOR. (**a**) 3D Bode phase plots and (**b**) Nyquist plots of D-NiCoO$_x$H$_y$-V$_{Cr,O}$ at various applied potentials in 1.0 M KOH with 0.1 M glycerol. (**c**) 3D Bode phase plots and (**d**) Nyquist plots of D-NiCoO$_x$H$_y$ under identical conditions.

Together, these in situ EIS results show that dual-vacancy engineering simultaneously optimizes bulk charge transport, accelerates interfacial charge transfer, and strengthens substrate adsorption, providing the kinetic basis for the excellent GOR performance of D-NiCoO$_x$H$_y$-V$_{Cr,O}$.

2.5. Studies on the Structure–Performance Relationship over D-NiCoO$_x$H$_y$-V$_{Cr,O}$

The structure–performance relationship of D-NiCoO$_x$H$_y$-V$_{Cr,O}$ in GOR was examined by HPLC and open-circuit potential (OCP) measurements. Across applied potentials of 1.26 to 1.42 V vs. RHE, glycerol conversion increases markedly with potential (Figure 5a), and at 1.32 V vs. RHE the yield, selectivity, and Faradaic efficiency of formic acid all approach 100%, demonstrating highly selective, directional conversion. The time-dependent concentration profiles (Figure S9) further verify that formic acid accumulates steadily with reaction time, while the concentrations of C_2 intermediates remain consistently low, confirming the rapid and selective C-C bond cleavage enabled by the dual-vacancy structure. Cyclic electrolysis at a constant charge of 77.2 C over eight consecutive cycles shows that the formate selectivity and Faradaic efficiency remain nearly unchanged (Figure 5b), confirming the excellent operational stability of D-NiCoO$_x$H$_y$-V$_{Cr,O}$ during glycerol electrooxidation. To further evaluate the long-term operational durability of D-NiCoO$_x$H$_y$-V$_{Cr,O}$, chronopotentiometry stability tests were conducted at a constant current density of 10 mA cm^{-2} in 1.0 M KOH with

0.1 M glycerol using a flow electrolyzer configuration. As shown in Figure S11, the catalyst exhibits a stable potential plateau over 84 h of continuous electrolysis, with only a negligible potential increase, demonstrating excellent long-term durability under practical operating conditions. Comparing the product distributions of D-$NiCoO_xH_y$-$V_{Cr,O}$ and D-$NiCoO_xH_y$ (Figure S10) shows that D-$NiCoO_xH_y$-$V_{Cr,O}$ converts glycerol more efficiently, whereas D-$NiCoO_xH_y$ generates substantially more by-products such as oxalic acid and glyceraldehyde, indicating that the coupled vacancies suppress side reactions and promote selective conversion to formic acid. The corresponding HPLC chromatograms for D-$NiCoO_xH_y$-$V_{Cr,O}$ (Figure S8) also confirm the disappearance of the glycerol peak and the dominant formate signal over time. Open-circuit potential (OCP) measurements (Figure 5c) show that injecting 0.1 M glycerol into the 1 M KOH electrolyte at 100 s produces a potential drop of 73.3 mV for D-$NiCoO_xH_y$-$V_{Cr,O}$, compared with only 4.5 mV for D-$NiCoO_xH_y$, suggesting enhanced glycerol adsorption interaction on the defect-modulated catalyst surface. Multi-potential-step chronoamperometry (Figure 5d) shows a rapid, pronounced current response upon glycerol injection at each potential, confirming the strong electrocatalytic activity and fast electron transfer kinetics of D-$NiCoO_xH_y$-$V_{Cr,O}$. Based on the product analysis, we propose a reaction pathway in which glycerol is first dehydrogenated to glyceraldehyde and then oxidized to glyceric acid (GLA), from which C-C bond cleavage generates formic acid together with glycolic acid (GCA). GCA is further oxidized via glyoxylic acid to formic acid (Figure 5e).

Collectively, the HPLC, in situ spectroscopic, and electrochemical results show that the dual-vacancy structure of D-$NiCoO_xH_y$-$V_{Cr,O}$ couples enhanced substrate adsorption with selective C-C bond activation. V_M-induced electronic modulation of the active metal sites improves glycerol mass transfer and conversion, while V_O drives directional C-C bond cleavage toward formic acid. Together, these effects give D-$NiCoO_xH_y$-$V_{Cr,O}$ its high activity and selectivity, and establish vacancy engineering as an effective strategy for designing selective biomass electrooxidation catalysts.

2.6. In Situ FTIR Spectroscopic Evidence for the Reaction Pathway

To corroborate the proposed reaction pathway (Figure 5e), in situ electrochemical attenuated total reflection Fourier-transform infrared (ATR-FTIR) spectroscopy was employed. Figure 6a displays the potential-dependent in situ FTIR spectra of the defect-rich D-$NiCoO_xH_y$-$V_{Cr,O}$ catalyst. Upon stepping the potential from OCP to 1.8 V vs. RHE, the characteristic absorption bands of FA are clearly observed, specifically the symmetric ν(O-C-O) stretching vibration at ~1340–1385 cm^{-1} and the asymmetric ν_{as} (O-C-O) vibration at ~1576 cm^{-1} [61]. Notably, these FA peaks increase in intensity and dominate the spectra with rising potentials. Meanwhile, the characteristic ν(C-O) vibration of glyceraldehyde (GLAD) at ~1050 cm^{-1} is essentially undetectable, whereas transient peaks corresponding to glycolic acid (GCA) at ~1058 cm^{-1} and glyceric acid (GLA) at ~1428 cm^{-1} are observable during the reaction process [16].

In striking contrast, the in situ FTIR spectra of the vacancy-poor D-$NiCoO_xH_y$ control catalyst (Figure 6b) reveal a prominent and persistent accumulation peak of GLAD at ~1070 cm^{-1} accompanied by relatively weak FA features. This stark difference demonstrates that without the synergistic coupling of metal and oxygen vacancies, the reaction is kinetically trapped at the GLAD intermediate stage due to sluggish C-C bond cleavage. However, for D-$NiCoO_xH_y$-$V_{Cr,O}$, the generated V_O promotes the formation of active V_O-OH_{ads} intermediates, which serve as critical reactive species to facilitate C-C bond cleavage. Meanwhile, the V_M enhances the local electron deficiency of the active Ni^{3+}/Co^{3+} sites, favoring the initial adsorption of glycerol. Consequently, the dual-vacancy structure effec-

tively drives the reaction along the GLA → GCA pathway while simultaneously avoiding the accumulation of by-products. The rapid conversion of unstable glyoxylic acid yields the nearly 100% selectivity toward formate, fully consistent with the HPLC and Faradaic efficiency results.

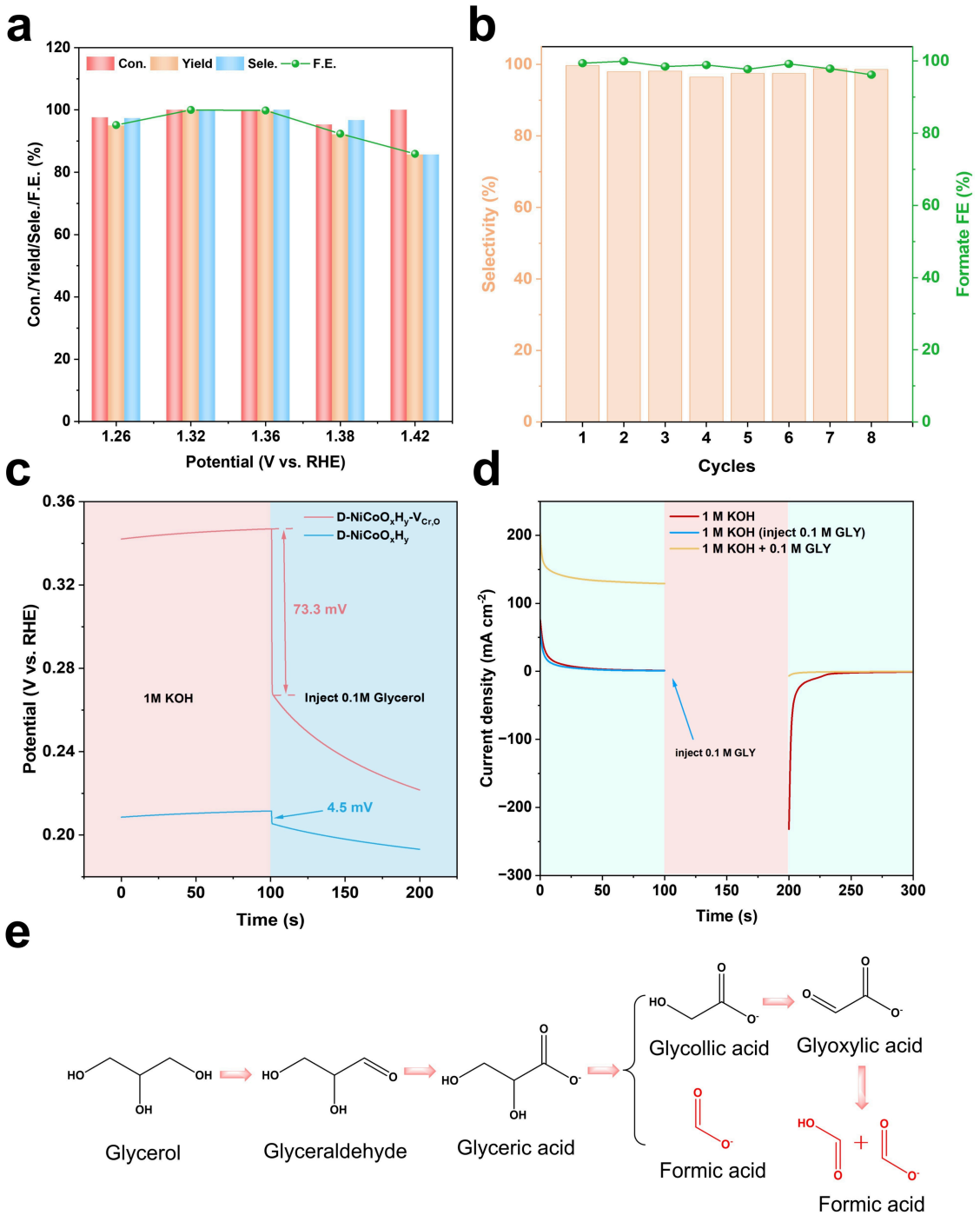


Figure 5. Structure–performance relationship of D-NiCoO$_x$H$_y$-V$_{Cr,O}$ in GOR. (**a**) Conversion, yield, selectivity, and Faradaic efficiency (F.E.) for formic acid across 1.26 to 1.42 V vs. RHE. (**b**) Cyclic stability over eight consecutive electrolysis cycles, showing formic acid selectivity and F.E. (1.32 V vs. RHE) (**c**) Open-circuit potential (OCP) curves of D-NiCoO$_x$H$_y$-V$_{Cr,O}$ and D-NiCoO$_x$H$_y$ in 1.0 M KOH before and after injecting 0.1 M glycerol at 100 s. (**d**) Chronoamperometric (CA) responses upon addition of 0.1 M glycerol. (**e**) Proposed reaction pathway for glycerol electrooxidation.

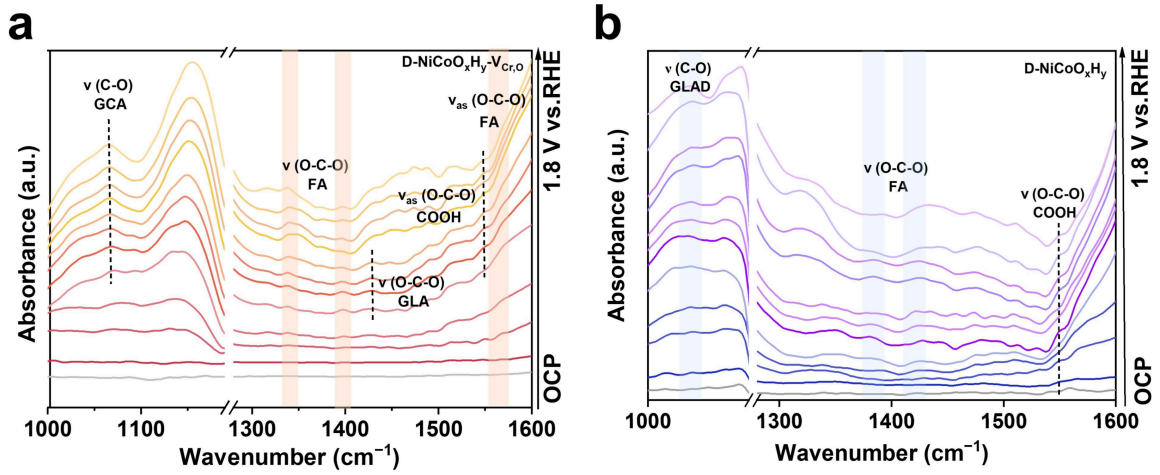


Figure 6. (**a**) In situ electrochemical ATR-FTIR spectroscopy over D-NiCoO$_x$H$_y$-V$_{Cr,O}$ at varied potentials. (**b**) In situ electrochemical ATR-FTIR spectroscopy over D-NiCoO$_x$H$_y$ at varied potentials.

3. Experimental Section

3.1. Chemicals and Materials

Cobalt nitrate hexahydrate (Co(NO$_3$)$_2$·6H$_2$O) and chromium nitrate nonahydrate (Cr(NO$_3$)$_3$·9H$_2$O) were purchased from Thermo Fisher (Shanghai, China) Scientific Co., Ltd. Potassium hydroxide (KOH) and hydrochloric acid (HCl) were purchased from Tianjin Fuyu Fine Chemical (Tianjin, China). Nickel foam (NF) was purchased from Suzhou Sinero Technology Co., Ltd. (Suzhou, China). Ethanol (C$_2$H$_6$O) and acetone (C$_3$H$_6$O) were purchased from Sinopharm Chemical Reagent Co., Ltd. (Shanghai, China). All chemicals were of reagent grade and used without further purification.

3.2. Synthesis of D-NiCoO$_x$H$_y$-V$_{Cr,O}$

The nickel foam (NF, 1.0 cm × 2.0 cm) substrate was first cleaned in an ultrasound bath with 3 mol/L HCl, acetone, deionized (DI) water, and ethanol successively (the same cleaning procedure was used for all substrates described below). Ni(NO$_3$)$_2$·6H$_2$O (1.047 g), Co(NO$_3$)$_2$·6H$_2$O (1.048 g), and Cr(NO$_3$)$_3$·9H$_2$O (1.441 g) were dissolved in 30 mL of deionized water and stirred for 5 min in a 50 mL beaker. The cleaned NF was mounted on the electrode clamp, immersed in the prepared solution, and polarized at a constant potential of −1.0 V vs. Ag/AgCl for 600 s at room temperature. During this process, partial dissolution of the NF substrate provides Ni^{2+} ions that combine with Co^{2+}, Cr^{3+}, and OH^- ions to form NiCoCrO$_x$H$_y$ on the NF surface. The resulting NiCoCrO$_x$H$_y$ sample was then removed, rinsed with DI water and ethanol, and dried at 60 °C overnight.

The NiCoCrO$_x$H$_y$ sample was then soaked in 10 mL of 1.0 mol/L KOH at room temperature and activated by cyclic voltammetry in 1.0 M KOH within a potential window of −0.1 to 0.8 V vs. Hg/HgO at a scan rate of 50 mV s^{-1} for 50 cycles, inducing structural reconstruction through hydroxyl interaction with the metal sites. The resulting product was ultrasonically washed several times with DI water and dried under vacuum at 60 °C overnight to afford D-NiCoO$_x$H$_y$-V$_{Cr,O}$ for characterization and catalytic testing.

3.3. Synthesis of D-NiCoO$_x$H$_y$

To evaluate the effect of Cr doping on GOR performance, a Cr-free control catalyst containing only Ni and Co was prepared under otherwise identical conditions. Ni(NO$_3$)$_2$·6H$_2$O (1.047 g) and Co(NO$_3$)$_2$·6H$_2$O (1.048 g) were dissolved in 30 mL of deionized water and stirred for 5 min in a 50 mL beaker. The cleaned NF was mounted on the electrode clamp, immersed in the prepared solution, and polarized at a constant potential of −1.0 V vs.

RHE for 600 s at room temperature. The resulting $NiCoO_xH_y$ sample was removed, rinsed with DI water and ethanol, and dried at 60 °C overnight. The $NiCoO_xH_y$ sample was then soaked in 10 mL of 1.0 mol/L KOH at room temperature and activated by cyclic voltammetry, followed by ultrasonic washing with DI water and drying at 60 °C overnight to afford D-$NiCoO_xH_y$ for catalytic testing.

3.4. Electrochemical Measurements

All electrochemical measurements were conducted on a CORRTEST electrochemical workstation (model CS310MA) using a standard three-electrode system in a 1.0 M KOH electrolyte (pH = 13.8) within a standard two-compartment H-cell separated by a Nafion 117 membrane. Each compartment had a volume of 10 mL and was filled with 10 mL of electrolyte. The working electrode compartment contained 1.0 M KOH with 0.1 M glycerol while the counter electrode compartment was filled with 1.0 M KOH. A standard Hg/HgO electrode and a graphite electrode were used as the reference and counter electrodes, respectively. The distance between the working and counter electrodes was approximately 5.0 cm. Nickel foam (NF, thickness of 1 mm) with self-supported active catalysts served as the working electrode. The geometric working area of the nickel foam electrode was fixed at 1.0×1.0 cm^2 (1.0 cm^2). All measured potentials were converted to the reversible hydrogen electrode (RHE) using the following equation: $E_{RHE} = E_{Hg/HgO} + 0.098 + 0.059 \times pH$. All data provided in this work were iR-corrected (80% iR compensation) according to the equation: $E_{compensated} = E_{measured} - iR$, where $E_{compensated}$ is the compensated potential, $E_{measured}$ is the measured potential, and R is the equivalent series resistance determined by the current interruption technique.

Linear sweep voltammetry (LSV) polarization curves were recorded in a 1.0 M KOH solution at a scan rate of 5 mV s^{-1}. Prior to the LSV measurements, 50 cycles of cyclic voltammetry (CV) were performed to stabilize the current. The Tafel slope was determined from the LSV data. Similarly, in-situ EIS was performed on the same workstation at various potentials (1.0, 1.05, 1.1, 1.15, 1.2, 1.25, 1.3, 1.35, 1.4, 1.45, 1.5, 1.55, 1.6) with identical and frequency range settings. The electrochemical surface area (ECSA) was assessed by measuring the electrochemical double-layer capacitance (Cdl), derived from a series of CV curves at different scan rates (20, 40, 60, 80, 80 and 100 mV s^{-1}) within a potential range of 0.86 to 0.96 V vs. RHE. The ECSA was represented by the slope of the linear fit of $\Delta J = Ja - Jc$ at the scan rate at 0.91 V vs. RHE, where Ja is the anodic current density and Jc is the cathodic current density.

3.5. Product Analysis

The oxidation products of glycerol during the electrolysis process were monitored using high-performance liquid chromatography (HPLC, 1260 Infinity II, Agilent, Santa Clara, CA, USA). Quantification was performed using external standard calibration curves for glycerol, oxalic acid, and formic acid (Figures S12–S14), with detection limits listed in the Supporting Information. A 5 Mm H_2SO_4 solution served as the mobile phase at flow rate of 0.5 mL min^{-1}. The electrolyte (10 μL) was directly injected into an Agilent Technologies Hi-Plex H column at 25 °C, and the products were identified by comparing their retention times with those of corresponding reference standards. The yield of the oxidation product was obtained according to the following equation:

$$Yield(\%) = \frac{mole\ of\ oxidation\ product}{mole\ of\ initial\ glycerol} \times 100 \quad (1)$$

The Faraday efficiency (FE) was calculated using the following equation:

$$Faraday\ efficiency(\%) = \frac{mole\ of\ oxidation\ product \times n \times F}{total\ passed\ charge} \times 100 \quad (2)$$

where n represents the number of electrons transferred, and F is the Faraday constant.

4. Conclusions

In summary, coupling metal and oxygen vacancies in amorphous D-$NiCoO_xH_y$-$V_{Cr,O}$ modulates the local electronic environment of Ni and Co, raises their oxidation states, strengthens hydroxyl uptake, and promotes the generation of active oxygenated intermediates. These effects lower the reaction barrier, accelerate charge transfer, and enable preferential C-C bond cleavage while suppressing side reactions, allowing the catalyst to reach 200 mA cm^{-2} at only 1.31 V vs. RHE with a Faradaic efficiency of 100% and stable performance over repeated electrolysis cycles. This work provides a non-noble-metal catalyst for glycerol valorization and establishes vacancy coupling as a design principle for selective biomass electrooxidation.

Supplementary Materials: The following supporting information can be downloaded at: https://www.mdpi.com/article/10.3390/catal16080747/s1, Figure S1: XRD patterns of D-$NiCoO_xH_y$ and D-$NiCoO_xH_y$-$V_{Cr,O.}$; Figure S2: HRTEM images of D-$NiCoO_xH_y$-$V_{Cr,O}$; Figure S3: The LSV curves of the high-Cr, less-Cr samples, bare Ni foam (NF), and D-$NiCoO_xH_y$-$V_{Cr,O}$ in 1.0 M KOH + 0.1 M glycerol, recorded at a scan rate of 5 mV s^{-1} (80% iR-corrected); Figure S4: CV curves of (a) D-$NiCoO_xH_y$-$V_{Cr,O}$ and (b) D-$NiCoO_xH_y$ at different scan rates for double-layer capacitance measurement; Figure S5: ECSA normalized LSV curves of D-$NiCoO_xH_y$-$V_{Cr,O}$ and D-$NiCoO_xH_y$ for GOR; Figure S6: Repeated polarization curves (n = 3) of D-$NiCoO_xH_y$-$V_{Cr,O}$ in 1.0 M KOH + 0.1 M glycerol. (No iR-corrected); Figure S7: Repeated polarization curves (n = 3) of D-$NiCoO_xH_y$ in 1.0 M KOH + 0.1 M glycerol. (No iR-corrected); Figure S8: Time-resolved HPLC chromatograms of glycerol electrooxidation over D-$NiCoO_xH_y$-$V_{Cr,O}$; Figure S9: Concentration evolution of reactant and products during glycerol electrooxidation over D-$NiCoO_xH_y$-$V_{Cr,O}$; Figure S10: Product selectivity comparison between D-$NiCoO_xH_y$-$V_{Cr,O}$ and D-$NiCoO_xH_y$ for glycerol electrooxidation; Figure S11: Stability test of D-$NiCoO_xH_y$-$V_{Cr,O}$ in the flow electrolyzer at 10 mA cm^{-2}; Figure S12: Calibration curves for glycerol (GLY) using high-performance liquid chromatography (HPLC); Figure S13: Calibration curves for oxalic acid (OA) using high-performance liquid chromatography (HPLC); Figure S14: Calibration curves for formic acid (FA) using high-performance liquid chromatography (HPLC); Table S1: Peak-fitting results of Ni 2*p* and Co 2*p* of XPS spectra for the D-$NiCoO_xH_y$-$V_{Cr,O}$ and D-$NiCoO_xH_y$ after GOR; Table S2: The resistance of each component for D-$NiCoO_xH_y$-$V_{Cr,O}$ in 1 M KOH with 0.1 M GLY; Table S3: The resistance of each component for D-$NiCoO_xH_y$ in 1 M KOH with 0.1 M GLY. etc.

Author Contributions: Z.S. and Y.F. contributed equally to this work and performed the experiments, characterization, and data analysis. G.L., J.M., R.M. and W.Y. assisted with catalyst characterization and electrochemical testing. M.X. and T.C. conceived and supervised the project and revised the manuscript. All authors have read and agreed to the published version of the manuscript.

Funding: This work was supported by the National Natural Science Foundation of China (No. 22379023, No. 22572021); the Heilongjiang Provincial Natural Science Foundation Outstanding Youth Fund Project (YQ2025B002); the National Key Research and Development Program (2024YFD2201503); the China Postdoctoral Science Foundation (No. 2025M771070, 2025T180292); the Heilongjiang Provincial Postdoctoral Science Foundation (LBH-Z24003); the Heilongjiang Provincial Key Research and Development Program Guidance Category Project (GZ20220073, GZ2024012); The Undergraduate Training Programs for Innovations by NEFU [grant number S202510225266].

Data Availability Statement: The data presented in this study are available on request from the corresponding author due to ongoing patent protection and confidentiality of proprietary synthesis methods.

Acknowledgments: We also thank the Large-Scale Instrument and Equipment Sharing Service Platform of the College of Chemistry, Chemical Engineering and Resource Utilization, NEFU, for supporting XRD tests.

Conflicts of Interest: The authors declare no conflicts of interest.

References

1. Song, M.; Bai, Y.; Li, J.; Qi, X. Efficient strategies for the preparation of non-noble metal catalysts for electrocatalytic glycerol oxidation towards high-value-added chemicals. *RSC Adv.* **2025**, *15*, 20513–20529. [CrossRef] [PubMed]
2. Pagliaro, M.; Ciriminna, R.; Kimura, H.; Rossi, M.; Della Pina, C. From glycerol to value-added products. *Angew. Chem. Int. Ed.* **2007**, *46*, 4434–4440. [CrossRef] [PubMed]
3. Katryniok, B.; Kimura, H.; Skrzyńska, E.; Girardon, J.-S.; Fongarland, P.; Capron, M.; Ducoulombier, R.; Mimura, N.; Paul, S.; Dumeignil, F. Selective catalytic oxidation of glycerol: Perspectives for high value chemicals. *Green Chem.* **2011**, *13*, 1960–1979. [CrossRef]
4. Luo, H.; Barrio, J.; Sunny, N.; Li, A.; Steier, L.; Shah, N.; Stephens, I.E.L.; Titirici, M. Progress and perspectives in photo- and electrochemical-oxidation of biomass for sustainable chemicals and hydrogen production. *Adv. Energy Mater.* **2021**, *11*, 2101180. [CrossRef]
5. Li, C.; Azam, T.; Li, S.; Fu, Y.; Zhang, M.; Wang, X.; Zhou, Y.J.; Wu, Z. Electrooxidation of glycerol to formic acid: From catalyst design strategies to key coupled systems. *ChemSusChem* **2025**, *18*, e202500220. [CrossRef] [PubMed]
6. Yoon, K.-Y.; Hwang, S.W.; Roh, H.Y.; Gu, J.; Lee, K.-B.; Jeong, J.; Oh, D.; Kwak, M.-J.; Yu, J.M.; Kim, D.; et al. Commercial-scale glycerol valorization using surface-modified copper cobalt oxide catalyst in high-capacity anion exchange membrane electrolyzer. *Joule* **2026**, *10*, 102303. [CrossRef]
7. Li, Y.; Yin, L.; Liu, J.; Qin, X.; Lu, X.; Dai, X.; Qi, K.; Yang, Y.; Qi, W.; Liu, G. Efficient glycerol electro-oxidation at an industrial-level current density. *Nat. Sustain.* **2025**, *8*, 1524–1532. [CrossRef]
8. Liu, Y.-B.; Chiang, C.-Y. Insights into the electrochemical valorization of glycerol under industrially relevant current densities: Roles of electrolyte engineering and the depletion effect. *Chem. Eng. J.* **2025**, *507*, 160619. [CrossRef]
9. Gaines, R.N.; Sibal, A.P.; Bradley, A.M.; Griebler, J.J.; Shah, V.M.; Friel, B.E.; Rogers, S.A.; Stillwell, A.S.; Kenis, P.J.A. Electrolysis for valorization of industrially-sourced crude glycerol. *ACS Sustain. Chem. Eng.* **2025**, *13*, 13250–13260. [CrossRef]
10. Li, H.; Kong, Y.; Zhao, Y.; Yu, P.; Zheng, Y.; Liu, Q.; Zhan, Q.; Wei, Y.; Ma, T.; Li, S. Tiny high-entropy doping strategy in CoNi-based MOF catalysts for selective glycerol electrooxidation to formic acid. *J. Energy Chem.* **2026**, *119*, 898–907. [CrossRef]
11. Luo, W.; Li, Q.; Tian, H.; Ma, J.; Yang, T.; Li, M.; Wu, H.; Kong, F.; Cui, X.; Shi, J. Bioinspired catalyst/electrolyte interfacial hydrogen-bond network engineering toward proton transfer acceleration for glycerol electrooxidation. *J. Am. Chem. Soc.* **2026**, *148*, 11099–11111. [CrossRef] [PubMed]
12. Yu, Y.; Wang, Y.; Ye, H.; Halder, S.; Yang, G.; Ye, B.; Kumar, S.; Held, G.; Durrant, J.R.; Titirici, M.-M.; et al. Mechanistic study of glycerol electro-oxidation on $Ni(OH)_2$/NiOOH electrodes. *J. Am. Chem. Soc.* **2026**, *148*, 16119–16128. [CrossRef] [PubMed]
13. Sun, F.; Liu, G.; Nie, T.; Wu, Z.; Hu, Y.; Song, Z.; Song, Y.-F. Synergistic band gap narrowing and interfacial electron flow in Pd-embedded NiCo-LDH for high-efficiency glycerol electrooxidation. *ACS Catal.* **2025**, *15*, 17513–17524. [CrossRef]
14. Cao, W.; Shen, Z.; Li, J.; Li, J.; Zhao, Y.; Zhang, Q.; Liu, Q. Efficient electrocatalysis conversion of glycerol to formate in alkaline solution by nickel (oxy)hydroxide supported cobalt nanoneedle arrays. *J. Colloid Interface Sci.* **2025**, *682*, 242–250. [CrossRef] [PubMed]
15. Lee, H.; Cha, J.; Cha, S.G.; Kong, T.-H.; Park, N.; Kwon, S.; Kim, H.J.; Kwon, Y. Foreign cation-promoted active species formation enables efficient electrochemical glycerol valorization. *Chem. Commun.* **2025**, *61*, 8011–8014. [CrossRef] [PubMed]
16. Chen, H.; Gao, R.; Su, K.; Li, Z.; Wu, L.; Wang, L. Re and Ru co-doped transition metal alloy as a bifunctional catalyst for electrooxidation of glycerol to formate coupled with H_2 production. *Angew. Chem. Int. Ed.* **2025**, *64*, e202501766. [CrossRef] [PubMed]
17. Li, C.; Li, H.; Zhang, B.; Li, H.; Wang, Y.; Wang, X.; Das, P.; Li, Y.; Wu, X.; Li, Y.; et al. Efficient electrocatalytic oxidation of glycerol to formate coupled with nitrate reduction over Cu-doped NiCo alloy supported on nickel foam. *Angew. Chem. Int. Ed.* **2024**, *63*, e202411542. [CrossRef] [PubMed]
18. Huang, C.; Lu, J.; Zeng, C.; Zhao, K.; Yang, S.; Deng, B.; Liu, Y. Ternary CuCoMo amorphous alloy enabling selective glycerol electrooxidation coupling with hydrogen evolution. *ACS Sustain. Chem. Eng.* **2025**, *13*, 12605–12614. [CrossRef]
19. Liu, Z.; Li, W.; He, J.; Wang, Z.; Liu, Y.; Wang, P.; Cheng, H.; Dai, Y.; Huang, B.; Zheng, Z. Boosting electrocatalytic glycerol oxidation into formate by enhancing glycerol adsorption via Pt-$NiCo_2O_4$ catalysts. *Appl. Surf. Sci.* **2026**, *736*, 166782. [CrossRef]
20. Xia, Z.; Ma, C.; Fan, Y.; Lu, Y.; Huang, Y.-C.; Pan, Y.; Wu, Y.; Luo, Q.; He, Y.; Dong, C.-L.; et al. Vacancy optimized coordination on nickel oxide for selective electrocatalytic oxidation of glycerol. *ACS Catal.* **2024**, *14*, 1930–1938. [CrossRef]

21. Guo, Y.; Xu, Y.; Chen, P. Ampere-level glycerol electrooxidation enabled by oxygen vacancy-riched crystalline/amorphous Co_3O_{4-x}/ZrO_{2-x} heterointerface. *J. Colloid Interface Sci.* **2025**, *699*, 138292. [CrossRef] [PubMed]
22. Zhong, S.; Zaidi, S.A.H.; He, B.; Wei, S.; Nawaz, H.; Wang, R.; Liu, R. "Vacancy mediated internal-external synergy" regulation strategy on constructing defect-engineered non-noble metal catalysts for electrooxidation of glycerol. *Chem. Eng. J.* **2025**, *519*, 165278. [CrossRef]
23. Ren, H.; Cai, G.; Guo, J.; Sun, Y.; Yao, W.; Ye, D.; Qian, H.; Zhang, J.; Zhao, H. Tuning the adsorption sites of OH− in glycerol electro-oxidation via oxygen vacancies on cobalt (II) oxide to promote electrocatalytic performance. *Small* **2025**, *21*, e07244. [CrossRef] [PubMed]
24. Niu, H.-J.; Ran, N.; Zhou, W.; An, W.; Huang, C.; Chen, W.; Zhou, M.; Lin, W.-F.; Liu, J.; Guo, L. Synergistic atomic environment optimization of nickel–iron dual sites by Co doping and Cr vacancy for electrocatalytic oxygen evolution. *J. Am. Chem. Soc.* **2025**, *147*, 2607–2615. [CrossRef] [PubMed]
25. Zhai, Y.; Ren, X.; Gan, T.; She, L.; Guo, Q.; Yang, N.; Wang, B.; Yao, Y.; Liu, S. Deciphering the synergy of multiple vacancies in high-entropy layered double hydroxides for efficient oxygen electrocatalysis. *Adv. Energy Mater.* **2025**, *15*, 2502065. [CrossRef]
26. Rafei, M.; Piñeiro-García, A.; Wu, X.; Puentes-Prado, E.; Ustunel, T.; Appelfeller, S.; Wågberg, T.; Gracia-Espino, E. Distorted octahedral sites drive early formation and stabilisation of nickel oxyhydroxides in trimetallic nickel–iron–molybdenum oxides. *Commun. Mater.* **2025**, *6*, 115. [CrossRef]
27. Zhao, J.; Li, X.; Wang, K.; Hung, Y.-T.; Wang, Q.; Cui, X.; Gao, G.; Li, X.; Liu, R.-S.; Zhao, X. Engineering Co-ion vacancy in dynamically reconstructed Co-based catalysts for practical anion-exchange membrane electrolysis. *Nat. Commun.* **2026**, *17*, 2858. [CrossRef] [PubMed]
28. Zhang, Q.; Zhang, X.; Liu, B.; Jing, P.; Xu, X.; Hao, H.; Gao, R.; Zhang, J. Active hydroxyl-mediated preferential cleavage of carbon-carbon bonds in electrocatalytic glycerol oxidation. *Angew. Chem. Int. Ed.* **2025**, *64*, e202420942. [CrossRef] [PubMed]
29. Li, J.; Zhang, Y.; Zhang, L.; Zhou, Q.; Yang, J.; Fu, Y.; Yu, L.; Sun, Y.; Li, Z.; Qin, Y.; et al. Facilitating OH* generation on atomic Pd–Cu dual sites towards efficient glycerol electrooxidation to formate. *Angew. Chem. Int. Ed.* **2025**, *64*, e202425006. [CrossRef] [PubMed]
30. Han, S.; Liu, B. Robust formate electrosynthesis from mixed biomass polyols by a direct carbon–carbon bond cleavage route. *J. Am. Chem. Soc.* **2026**, *148*, 778–789. [CrossRef] [PubMed]
31. Zhang, Y.; Zhang, Y.; Wei, H.; Li, J.; Sun, Z.; Chen, W.; Zhang, Z. Selective adsorption–oxidation of glycerol to formate at Ni–O–Ce nanoheterointerfaces. *Nano Lett.* **2026**, *26*, 4497–4506. [CrossRef] [PubMed]
32. Wang, S.; Tong, Z.; Li, Y.; Lin, Y.; Wang, J.; Tian, Z.; Yin, H.; Chen, L. Preferential cleavage of C–C bonds in glycerol electrooxidation via multi-site collaboration within ultrathin medium-entropy nanosheets. *ACS Appl. Nano Mater.* **2026**, *9*, 5810–5824. [CrossRef]
33. Wu, W.; Cao, Z.; Huai, A.; Long, Y.; Liu, H.; Xue, C.; Liu, D.; Huang, W. Potential-controlled electrocatalytic glycerol reforming over nickel-based conductive metal–organic framework for switchable formate and oxalate production. *Appl. Surf. Sci.* **2026**, *743*, 167314. [CrossRef]
34. Wang, S.; Lin, Y.; Li, Y.; Tian, Z.; Wang, Y.; Lu, Z.; Ni, B.; Jiang, K.; Yu, H.; Wang, S.; et al. Nanoscale high-entropy surface engineering promotes selective glycerol electro-oxidation to glycerate at high current density. *Nat. Nanotechnol.* **2025**, *20*, 646–655. [CrossRef] [PubMed]
35. Jin, D.; Li, T.; Xu, J.; Hou, J. Breaking activity-stability trade-off by switching reaction pathway for efficient electrosynthesis of glycerate at industrial-scale current density. *Angew. Chem. Int. Ed.* **2026**, *65*, e3574115. [CrossRef] [PubMed]
36. Khan, A.R.; Kumari, B.; Wegner, J.; Pedrini, F.; Adofo, L.A.; Olean-Oliveira, A.; Hagemann, U.; Kleszczynski, S.; Andronescu, C.; Čolić, V. Glycerol electrooxidation at structured nickel electrodes and the effect of geometry on the selectivity of product. *ChemElectroChem* **2025**, *12*, e202500175. [CrossRef]
37. Xu, L.; Geng, S. Copper-doped NiOOH for the electrocatalytic conversion of glycerol to formate via the inhibition of the oxygen evolution reaction. *Inorg. Chem.* **2025**, *64*, 617–626. [CrossRef] [PubMed]
38. Long, B.; Zhang, Q.; Yang, M.; Li, Y.; Liu, H.; He, D.; Li, W.; Ke, Z.; Xiao, X. Enhanced glycerol electrooxidation capability of NiO by suppressing the accumulation of Ni^{4+} sites. *ACS Appl. Mater. Interfaces* **2025**, *17*, 13794–13803. [CrossRef] [PubMed]
39. Xu, L.; Geng, S. High-current-density glycerol electrooxidation on S–Cu–Ni/NF catalyst: Unveiling the synergy between S-promoted GOR and Cu-inhibited OER. *ACS Appl. Mater. Interfaces* **2025**, *17*, 30932–30942. [CrossRef] [PubMed]
40. Shi, L.; Cai, W.; Zhang, F.; Li, S.; Liu, X.; Liu, Y.; Ren, P.; Li, B.; Liu, S.; Liu, B. Engineering oxygen intermediates adsorption on amorphous NiFe alloys for highly active and selective electrochemical biomass conversion. *Angew. Chem. Int. Ed.* **2025**, *64*, e202424345. [CrossRef] [PubMed]
41. Ma, J.; Wang, X.; Song, J.; Tang, Y.; Sun, T.; Liu, L.; Wang, J.; Wang, J.; Yang, M. Synergistic Lewis and Brønsted acid sites promote OH* formation and enhance formate selectivity: Towards high-efficiency glycerol valorization. *Angew. Chem. Int. Ed.* **2024**, *63*, e202319153. [CrossRef] [PubMed]

42. Wu, L.; Wu, Q.; Han, Y.; Zhang, D.; Zhang, R.; Song, N.; Wu, X.; Zeng, J.; Yuan, P.; Chen, J.; et al. Strengthening the synergy between oxygen vacancies in electrocatalysts for efficient glycerol electrooxidation. *Adv. Mater.* **2024**, *36*, 2401857. [CrossRef] [PubMed]
43. Tong, Z.; Li, J.; Lin, Y.; Wang, S.; Wang, J.; Tian, Z.; Chen, L. Stable glycerol electrooxidation to glycerate over 1000 hours on a hydroxyl-modulated PdNiMo alloy. *Adv. Mater.* **2026**, *38*, e23353. [CrossRef] [PubMed]
44. Liu, Y.; Shang, H.; Zhang, B.; Yan, D.; Xiang, X. Surface fluorination of $BiVO_4$ for the photoelectrochemical oxidation of glycerol to formic acid. *Nat. Commun.* **2024**, *15*, 8155. [CrossRef] [PubMed]
45. Ye, F.; Zhang, S.; Cheng, Q.; Long, Y.; Liu, D.; Paul, R.; Fang, Y.; Su, Y.; Qu, L.; Dai, L.; et al. The role of oxygen-vacancy in bifunctional indium oxyhydroxide catalysts for electrochemical coupling of biomass valorization with CO_2 conversion. *Nat. Commun.* **2023**, *14*, 2040. [CrossRef] [PubMed]
46. Qian, Q.; He, X.; Li, Z.; Chen, Y.; Feng, Y.; Cheng, M.; Zhang, H.; Wang, W.; Xiao, C.; Zhang, G.; et al. Electrochemical biomass upgrading coupled with hydrogen production under industrial-level current density. *Adv. Mater.* **2023**, *35*, 2300935. [CrossRef] [PubMed]
47. Chang, J.; Song, F.; Hou, Y.; Wu, D.; Xu, F.; Jiang, K.; Gao, Z. Molybdenum, tungsten doped cobalt phosphides as efficient catalysts for coproduction of hydrogen and formate by glycerol electrolysis. *J. Colloid Interface Sci.* **2024**, *665*, 152–162. [CrossRef] [PubMed]
48. Zhou, S.; Dai, Y.; Song, Q.; Lu, L.; Yu, X. Efficient bi-functional catalyst towards coupling glycerol oxidation and CO_2 reduction to achieve formic acid and formate production. *J. Electroanal. Chem.* **2024**, *957*, 118133. [CrossRef]
49. Liu, P.; Ma, H.; Qin, Y.; Li, J.; Li, F.; Ye, J.; Guo, Q.; Su, N.; Gao, C.; Xie, L.; et al. Enhancing C—C bond cleavage of glycerol electrooxidation through spin-selective electron donation in Pd–PdS_2–Cox heterostructural nanosheets. *Angew. Chem. Int. Ed.* **2025**, *64*, e202506032. [CrossRef] [PubMed]
50. Li, G.; Kong, X.; Zhao, X.; Zhang, J.; Zhao, Y.; Sun, Q.; Yang, D.; He, F.; Yang, P.; Zhang, J.; et al. Phosphorus vacancy-engineered ultrathin RuP nanosheets for accelerated and high-capacity N-ethylcarbazole hydrogen storage. *Angew. Chem. Int. Ed.* **2026**, *65*, e12754. [CrossRef] [PubMed]
51. Fang, Z.; Zhang, J.; Guo, M.; Qiu, C.; Kong, X.; Zhao, X.; Zhao, Y.; Yang, D.; He, F.; Sun, Q.; et al. Noble metal catalysts for methanol steam reforming: Advances and future directions for hydrogen production. *J. Mater. Chem. A* **2026**, *14*, 10505–10523. [CrossRef]
52. Yang, L.; Ma, Y.; Yu, J.; Arbiol, J.; Li, J.; Cabot, A. Organic oxidation-assisted hydrogen production: Glycerol electroreforming to formate on nickel diselenide nanoparticles. *J. Colloid Interface Sci.* **2025**, *700*, 138535. [CrossRef] [PubMed]
53. Dodekatos, G.; Schünemann, S.; Tüysüz, H. Recent advances in thermo-, photo-, and electrocatalytic glycerol oxidation. *ACS Catal.* **2018**, *8*, 6301–6333. [CrossRef]
54. Xu, X.; Wang, P.; Shi, Q.; Zhang, J.; Zheng, J.; Long, Y.-Z. High-entropy alloy nanofiber electrocatalysts for hydrogen production via coupled glycerol electrooxidation. *Electrochim. Acta* **2025**, *539*, 147058. [CrossRef]
55. Yin, Q.; Xie, X.; Xu, L.; Geng, S. Boosting electrocatalytic glycerol oxidation reaction to formate based on Mn-doped Ni_7P_3. *J. Alloys Compd.* **2025**, *1022*, 179867. [CrossRef]
56. Chen, W.; Shi, J.; Wu, Y.; Jiang, Y.; Huang, Y.; Zhou, W.; Liu, J.; Dong, C.; Zou, Y.; Wang, S. Vacancy-induced catalytic mechanism for alcohol electrooxidation on nickel-based electrocatalyst. *Angew. Chem. Int. Ed.* **2024**, *63*, e202316449. [CrossRef] [PubMed]
57. Lin, J.-A.; Roh, I.; Yang, P. Photochemical diodes for simultaneous bias-free glycerol valorization and hydrogen evolution. *J. Am. Chem. Soc.* **2023**, *145*, 12987–12991. [CrossRef] [PubMed]
58. Yu, J.; González-Cobos, J.; Dappozze, F.; Grimaldos-Osorio, N.; Vernoux, P.; Caravaca, A.; Guillard, C. First PEM photoelectrolyser for the simultaneous selective glycerol valorization into value-added chemicals and hydrogen generation. *Appl. Catal. B Environ.* **2023**, *327*, 122465. [CrossRef]
59. Liu, C.; Hirohara, M.; Maekawa, T.; Chang, R.; Hayashi, T.; Chiang, C.-Y. Selective electro-oxidation of glycerol to dihydroxyacetone by a non-precious electrocatalyst–CuO. *Appl. Catal. B Environ.* **2020**, *265*, 118543. [CrossRef]
60. Vo, T.-G.; Ho, P.-Y.; Chiang, C.-Y. Operando mechanistic studies of selective oxidation of glycerol to dihydroxyacetone over amorphous cobalt oxide. *Appl. Catal. B Environ.* **2022**, *300*, 120723. [CrossRef]
61. Song, Y.; Wan, X.; Miao, Y.; Li, J.; Ren, Z.; Jin, B.; Zhou, H.; Li, Z.; Shao, M. Blocking oxygen evolution reaction for efficient organic electrooxidation coupling hydrogen production by using layered double hydroxide rich in active oxygen. *Appl. Catal. B Environ. Energy* **2023**, *333*, 122808. [CrossRef]

Disclaimer/Publisher's Note: The statements, opinions and data contained in all publications are solely those of the individual author(s) and contributor(s) and not of MDPI and/or the editor(s). MDPI and/or the editor(s) disclaim responsibility for any injury to people or property resulting from any ideas, methods, instructions or products referred to in the content.